Two-dimensional photoacoustic imaging by use of Fourier-transform image reconstruction and a detector with an anisotropic response

Kornel P. Köstli and Paul C. Beard

Theoretical and experimental aspects of two-dimensional (2D) biomedical photoacoustic imaging have been investigated. A 2D Fourier-transform-based reconstruction algorithm that is significantly faster and produces fewer artifacts than simple radial backprojection methods is described. The image-reconstruction time for a 208 $\times$ 482 pixel image is $\sim$1 s. For the practical implementation of 2D photoacoustic imaging, a rectangular detector geometry was used to obtain an anisotropic detection sensitivity in order to reject out-of-plane signals, thereby permitting a tomographic image slice to be reconstructed. This approach was investigated by the numerical modeling of the broadband directional response of a rectangular detector and imaging of various spatially calibrated absorbing targets immersed in a turbid phantom. The experimental setup was based on a Q-switched Nd:YAG excitation laser source and a mechanically line-scanned Fabry–Perot polymer-film ultrasound sensor. For a 800 μm $\times$ 200 μm rectangular detector, the reconstructed image slice thickness was 0.8 mm up to a vertical distance of $z = 3.5$ mm from the detector, increasing thereafter to 2 mm at $z = 10$ mm. Horizontal and vertical spatial resolutions within the reconstructed slice were approximately 200 and 60 μm, respectively. © 2003 Optical Society of America

OCIS codes: 170.5120, 170.3010.

1. Introduction

Biomedical photoacoustic imaging is based on irradiating a soft-tissue volume with nanosecond laser pulses. Absorption of the laser pulses results in a rapid temperature rise of the irradiated volume. This is followed by rapid thermoelastic expansion leading to an initial stress distribution, which acts as a pulsed source of broadband ultrasonic waves. These propagate to the surface where they are detected by an array of ultrasound detectors. Assuming a homogeneous distribution of the tissue thermomechanical properties and acoustic propagation parameters, an image of the internally absorbed laser energy distribution can then be reconstructed from the detected time-resolved photoacoustic signals. The principal advantage of the technique is that image contrast is based largely on differences in tissue optical properties, and, because these are strongly dependent on tissue constituents and structure, it offers the prospect of differentiating between soft tissues that are indistinguishable when other imaging modalities are used. For example, the strong optical absorption of hemoglobin offers the potential for high-contrast imaging of microvessels,[1–3] which, owing to their relatively low echogenicity, can be difficult to observe with conventional ultrasound imaging. Among the potential clinical applications that could exploit this are the assessment of breast cancer tumors[4] and other soft-tissue abnormalities[5] characterized by local structural and functional changes in the microvasculature.

Biomedical photoacoustic imaging is generally a three-dimensional (3D) problem: The strong optical scattering exhibited by tissues results in a 3D distribution of photoacoustic sources, and these, owing to the geometry of anatomical structures of interest, tend to emit acoustic energy into a large solid angle. The most apparent solution is to detect the photoacoustic signals over an area of the tissue surface by use of a two-dimensional (2D) array of isotropic ultrasound detectors and to reconstruct a 3D image from the detected signals.[1,3,6,7] However, the high

The authors are with the Department of Medical Physics and Bioengineering, University College London, Shropshire House, 11-20 Capper Street, London WC1E 6JA, United Kingdom. P. C. Beard's e-mail address is pbeard@medphys.ucl.ac.uk.

Received 20 September 2002; revised manuscript received 6 January 2003.

0003-6935/03/101899-10$15.00/0

cost and formidable technical difficulties involved in implementing such arrays with sufficiently high channel counts for acceptable data-acquisition times present substantial disadvantages. As in conventional medical ultrasound imaging,[8] detecting the signals along a line on the tissue surface by use of a linear or curvilinear array[4] of detectors of anisotropic response and reconstructing a 2D tomographic slice image often presents a more practicable and cost-effective clinical implementation owing to the much lower number of elements required. This is particularly so if near-real-time data acquisition and image reconstruction are required.

In this paper 2D photoacoustic imaging by use of linear arrays is explored theoretically and experimentally. Subsection 2.A presents aspects of 2D image reconstruction: the inherent ambiguity that arises from reducing the problem to two dimensions and a rapid Fourier-transform-based image-reconstruction algorithm—the latter fulfills an important requirement, given the applicability of 2D photoacoustic imaging to real-time imaging. A key requirement for practical implementation is the use of a rectangular detector element geometry to provide an anisotropic response so that signals originating from sources situated outside the detection plane are rejected. The directional characteristics of such a receiver in response to broadband photoacoustic signals are numerically modeled in Subsection 2.B. An experimental arrangement, based on a mechanically line-scanned Fabry–Perot (FP) optical ultrasound sensor for simulating a linear array, is described in Subsection 3.A. This system was used to obtain photoacoustic signals from various absorbing targets immersed in turbid media. These experimental data were used to evaluate the Fourier-transform reconstruction algorithm (Subsection 3.B) and the geometrical parameters of the reconstructed image slice obtained with a rectangular detector geometry (Subsection 3.C).

2. Theory

A. Two-Dimensional Image Reconstruction

Photoacoustic imaging is generally of a 3D nature: Acoustic waves are emitted by a 3D distribution of elemental photoacoustic sources radiating into a 4π solid angle and detected over an external surface or a volume. From the time-dependent detected signals $p(x, y, z, t)$, the initial 3D source distribution $p_0(x, y, z)$ can be reconstructed. For the specific task of reconstructing a 2D image in the x–z detection plane (Fig. 1), from an array of detectors arranged along a line $y = 0$ in the x–y plane, the problem can be reduced to two dimensions by introduction of one of the following assumptions:

1. Two-dimensional source distribution: $p_0(x, y, z) = p_0(x, z)\ \delta(y)$. This implies that there are no sources situated outside the detection plane. It is unlikely to occur in biomedical imaging applications as, owing to strong optical scattering in tissues, a 3D source distribution is generally produced.
2. Two-dimensional source directivity: $p_0(x, y, z) = p_0(x, z)$. This implies that the source distribution is constant in the y direction and can therefore be regarded as being highly directional in the y–z plane. Signals emitted by sources outside the detection plane will therefore not contribute to the detected signal. For example, a line source orientated perpendicularly to the detection plane emitting cylindrical waves would fulfill this condition. Although conceivable in certain circumstances (e.g., an appropriately orientated blood vessel), it is, in general, an unrealistic situation.
3. Two-dimensional detector directivity: The detector geometry is chosen to provide an omnidirectional response in the detection plane but a highly directional response in the plane perpendicular to it. Signals from out-of-plane sources will therefore be rejected. This represents the most practically relevant approach.

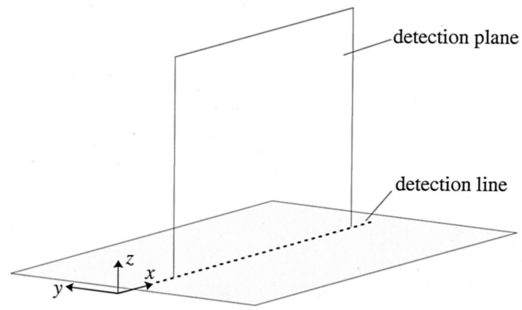

Fig. 1. Geometry for 2D image reconstruction.

Irrespective of their practical relevance, all three assumptions imply that no signals from out-of-plane sources are detected, and any of them could, in principle, be used in the formulation of a 2D image-reconstruction algorithm. For example, as shown later, it is mathematically expedient to employ assumption 2 when deriving the 2D Fourier-transform-based reconstruction algorithm even if it is assumption 3 that is invoked in practice. However, although assumptions 1 and 2 imply that no signals arrive at the detection line, they are not exactly equivalent. This highlights a specific ambiguity in 2D photoacoustic imaging. With assumption 1, $p_0(x, y, z) = p_0(x, z)\delta(y)$, the attenuation $a(r)$ of an acoustic signal originating from a point in the source distribution in the detection plane will, owing to the geometrical spreading of the emitted wave front, follow a $1/r$ dependence. With assumption 2, $p_0(x, y, z) = p_0(x, z)$, $a(r)$ is proportional to $1/\sqrt{r}$. In practice, the source geometry in the y direction is unknown. $a(r)$ could therefore be of a form that lies anywhere between these two extremes (i.e., a $1/r^n$ dependence, where $\frac{1}{2} < n < 1$); indeed, this uncertainty is implicit in assumption 3, which imposes no constraints on the source geometry. Because $a(r)$ is incorporated implicitly or explicitly in the image-reconstruction process, uncertainty in its form may compromise the fidelity of the reconstructed image in two ways. First, the source–detector distance is different for each point on the detected wave front, resulting in an $a(r)$-dependent distribution of amplitude along the wave front. This is equivalent to imposing an $a(r)$-dependent apodization function along the detection line, thus effectively modifying the aperture over which the wave front is sampled, with a consequent influence on the geometrical parameters (e.g., spatial resolution) of the reconstructed image. In practice, the directional sensitivity of the detectors often dominates this notional apodization function, and so the effect is of limited significance. The second consequence is that the relative amplitudes of sources at different distances from the detection line may be incorrectly assigned in the reconstructed image if $a(r)$ is unknown. The image will remain structurally correct, and so this effect will be of most consequence for applications that require a quantitatively accurate reconstruction.

With these limitations in mind, we can now proceed to consider the task of image reconstruction. First, consider the photoacoustic wave $p(\mathbf{r}, t)$ generated by the absorption of a laser pulse. We assume that the laser energy is deposited instantaneously within the target volume, producing an impulsive initial pressure source distribution—an important practical requirement for efficient photoacoustic generation. In practice, approximating to this condition requires that the laser pulse be sufficiently short (typically, of the order of nanoseconds) such that heat loss (due to thermal conduction) and dissipation of stress (due to acoustic propagation) from the irradiated target volume are insignificant over the laser-pulse duration. Assuming an acoustically linear and lossless propagation medium, the propagation of the photoacoustic wave $p(\mathbf{r}, t)$ can then be described by the 3D linear inhomogeneous acoustic wave equation with the time derivative of the initial impulsive pressure source distribution $p_0(\mathbf{r})\delta(t)$ as the source term [Eq. 1(a)].[9] Thus

$$\frac{\partial^2 p(\mathbf{r}, t)}{\partial^2 t} - c^2 \cdot \nabla^2 p(\mathbf{r}, t) = \frac{\partial}{\partial t} p_0(\mathbf{r})\delta(t), \tag{1a}$$

$$p_0(\mathbf{r}) = \Gamma \Psi(\mathbf{r}) \mu_a(\mathbf{r}), \tag{1b}$$

where the initial spatial distribution of pressure $p_0(\mathbf{r})$ is given by the product of the light fluence distribution $\Psi(\mathbf{r})$, the absorption coefficient of the tissue $\mu_a(\mathbf{r})$, and the dimensionless thermomechanical conversion factor Γ, the Grüneisen coefficient,[10] a measure of the efficiency of the conversion of heat energy to stress.

Equation (1) can be solved to yield[11]

$$p(\mathbf{r}, t) = \frac{1}{4\pi c} \frac{\partial}{\partial t} \int_{|\Delta \mathbf{r}| = ct} \frac{p_0(\mathbf{r} - \Delta \mathbf{r})}{ct} \mathrm{d}s. \tag{2}$$

Equation (2) states that the time-integrated acoustic pressure, or velocity potential, at a position $\mathbf{r}$ and time t, is the sum of all points in the initial pressure distribution that lie on a spherical surface s centered on $\mathbf{r}$ and of radius Δr equal to the product of the speed of sound c and t. This solution lends itself to the simplest approach to image reconstruction, whereby the time-dependent photoacoustic waveforms detected over the tissue surface are spatially resolved by use of the speed of sound and backprojected over hemispherical surfaces to obtain a 3D image of the initial pressure distribution.[3,7] Reducing this to two dimensions by use of any of the previous assumptions is straightforward, amounting to discarding the y spatial dependence, selecting an appropriate function to represent $a(r)$, and backprojecting over semicircles in the image plane. The disadvantages are long reconstruction times and the inevitable circular backprojection artifacts that arise from the indiscriminate nature of distributing the signal amplitude uniformly over an arc in the image plane.

An alternative approach is a reconstruction algorithm that uses a Fourier-transform method that has been developed for 3D photoacoustic imaging. The full details of the algorithm are described in Ref. 12, and its use for reconstructing 3D images from experimental data is described in Ref. 13. Briefly, it involves expressing the solution to Eq. (1), $p(\mathbf{r}, t)$, in terms of its spatial- and temporal-frequency components $\mathbf{k}$ and ω, respectively,

$$p(\mathbf{r}, t) = \frac{1}{(2\pi)^3} \int P(\mathbf{k}) \cos(\omega \cdot t) \exp(i \cdot k \cdot r) \mathrm{d}^3 k, \tag{3a}$$

with

$$\omega = c|\mathbf{k}| = c\sqrt{{k_x}^2 + {k_y}^2 + {k_z}^2}. \tag{3b}$$

For $t = 0$, the left-hand side of Eq. (3a) becomes equal to the initial pressure source distribution $p_0(\mathbf{r})$, $P(\mathbf{k})$ is therefore the 3D spatial Fourier transform of $p_0(\mathbf{r})$. By use of the dispersion relation of Eq. (3b) and an algebraic transform described in Ref. 12, $P(\mathbf{k})$ can be expressed in terms of the Fourier transform of the time-varying photoacoustic signals detected over the x–y plane and then inverse Fourier transformed to yield the desired initial pressure distribution $p_0(\mathbf{r})$. This method yields an exact 3D reconstruction, provided that the velocity c is constant and the measurements extend continuously over an infinite detection area and all times $t > 0$. Although in practice the measurements are spatially and temporally discretized over a finite detection area, the method can still be expected to provide an image with fewer artifacts than the simple backprojection approach, which never yields an exact reconstruction. An additional advantage is computational efficiency, largely through the use of the fast-Fourier-transform algorithm, providing a reduction in reconstruction times of at least 2 orders of magnitude compared with the backprojection method.

Reducing the Fourier-transform reconstruction method to two dimensions can be achieved most conveniently with assumption 2, $p_0(x, y, z) = p_0(x, z)$. In the spatial-frequency domain we can then write

$$P(\mathbf{k}) = P(k_x, k_z)\delta(k_y), \tag{4a}$$

$$\omega = c|\mathbf{k}| = c\sqrt{\mathbf{k}_x^{\,2} + \mathbf{k}_z^{\,2}}. \tag{4b}$$

We can now proceed to derive the 2D algorithm in a manner directly analogous to the 3D algorithm[12] to obtain $P(\mathbf{k})$ in terms of the Fourier transform $A(k_x, \omega)$ of the detected photoacoustic signals:

$$P\left[k_x, k_z = \sqrt{(\omega/c)^2 - k_x^{\,2}}\right] = \frac{2c\sqrt{\omega^2 - c^2 k_x^{\,2}}}{\omega} A(k_x, \omega), \tag{5a}$$

$$A(k_x, \omega) = \int_0^{\infty}\int_{-\infty}^{\infty} p(x, t)\exp(-ik_x x)\cos(\omega t)\mathrm{d}x\mathrm{d}t. \tag{5b}$$

By analogy with the 3D algorithm, this yields an exact reconstruction, providing that the source assumption, $p_0(x, y, z) = p_0(x, z)$, in addition to the requirements of continuous detection over an infinite line and all $t > 0$, is fulfilled.

From Eqs. (5a) and (5b), implementation of the algorithm therefore requires the following steps: (1) 2D Fourier transform the detected pressure signals to obtain $A(k_x, \omega)$, (2) scale each component of $A(k_x, \omega)$ by the expression in front of $A(k_x, \omega)$ in Eq. (5a). (3) transform ω into k_z by use of the dispersion relation of Eq. (4b) to obtain $P(k_x, k_z)$, and (4) inverse 2D Fourier transform $P(k_x, k_z)$ to recover the desired $p_0(\mathbf{r})$.

B. Directional Response of a Rectangular Detector

To reject out-of-plane signals as described in assumption 3, it is necessary to employ a rectangular detector geometry, ideally of length L and width w such that $L \gg \lambda$ and $w \ll \lambda$, where λ is the acoustic wavelength. This provides a highly directional response in the planes containing the length dimension of the detector but an omnidirectional response in the planes containing the width dimension. A line array of such detectors as depicted in Fig. 2 will therefore define a detection slice with only signals emanating from sources within this slice being detected. Although the slice is of finite thickness, we will continue to refer to sources within the slice as being in plane and those outside as being out of plane.

The detection slice thickness depends on the distance from the detector. In the nondivergent near-field receive zone close to the detector, it is approximately equal to L. Thereafter it increases linearly in accordance with the far-field directional response $F(\Theta)$ of the detector. For $L \gg w$ and angle Θ, this is given by[8]

$$F(\Theta) \propto \frac{\sin[\pi L \sin(\Theta/\lambda)]}{\pi L \sin[\Theta/\lambda]}. \tag{6}$$

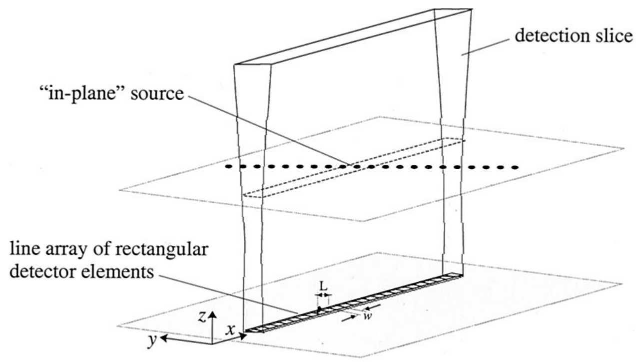

Fig. 2. Geometry of the detection slice defined by a line array of rectangular detector elements of length L and width w. The point sources that intersect the detection slice are termed in-plane sources, and the remaining sources are denoted out-of-plane sources.

Because expression Eq. (6) requires knowledge of the frequency content of the signal and pulsed photoacoustic signals are broadband, it is more convenient to model the directivity in the time domain. The source was numerically modeled by use of Eq. (2). To simulate the detector response F to an acoustic wave $p(\mathbf{r}, t)$ as a function of its geometry, we integrated Eq. (2) over the sensitive volume of the detector:

$$F(t) = \int_{\text{detector volume}} p(\mathbf{r}, t)\mathrm{d}^3 r = \int_{-\infty}^{\infty} p(\mathbf{r}, t) D(\mathbf{r})\mathrm{d}^3 r,$$

$$D(\mathbf{r}) = \begin{cases} 1 & \mathbf{r} \in \text{detector area} \\ 0 & \text{else} \end{cases}. \tag{7}$$

This means the pressure signal is calculated for each elemental volume $\mathrm{d}r^3$ within the detector and summed. To minimize computational expense, we can insert Eq. (2) into Eq. (7) and rearrange the integrals, leading to a convolution of the detector geometry and the pressure source, in essence, a statement of the principle of acoustic reciprocity:

$$F(t) = \frac{1}{4\pi c}\frac{\partial}{\partial t}\int_{|\Delta\mathbf{r}|=ct} \frac{D * p_0(\Delta\mathbf{r})}{ct}\mathrm{d}s,$$

where

$$D * p_0(\Delta\mathbf{r}) = \int_{-\infty}^{\infty} D(\mathbf{r}) p_0(\Delta\mathbf{r} - \mathbf{r})\mathrm{d}^3 r. \tag{8}$$

The algorithm based on Eq. (8) is now one in which the pressure source is convoluted or smeared with the geometry of the detector and the signal is calculated as if the detector was a point detector. This is substantially faster than an algorithm based on Eq. (7).

The model was used to examine the directional sensitivity of a rectangular detector element by modeling its output in response to acoustic waves emitted by a disk-shaped source of diameter 0.2 mm and thickness 20 μm situated at various positions within

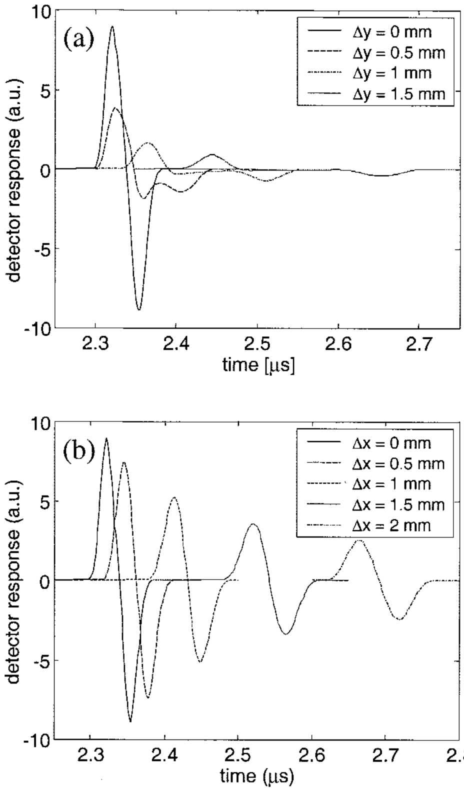

Fig. 3. Simulation of directional response of a single rectangular detector element that is due to a disk-shaped source of diameter 200 μm and thickness 20 μm aligned parallel to the x–y plane. The length dimension (L = 800 μm) of the detector is aligned parallel to the y axis, and the width dimension (w = 100 μm) is aligned parallel to the x axis. The thickness of the detector was 75 μm. The source is initially located directly above the detector at $x = y = 0$, $z = 3.5$ mm. (a) Detected signals as the source is translated in the y direction from this initial position. (b) Detected signals for the corresponding translations in the x direction.

the x–y plane. The disk is assumed to lie parallel to the x–y plane. The geometry of Fig. (2) is assumed with the length dimension L of the detector aligned parallel to the y axis and the width dimension w parallel to the x axis. The dimensions of the detector were L = 800 μm, w = 100 μm, and the thickness = 75 μm, those of FP polymer-film detector used in the experiments described in Section 3 below. To take into account the sound velocity in the detector of 2200 m/s, compared with water c = 1500 m/s, we reduced the thickness in the model to 75 μm × 1.5/2.2 = 50 μm (termed the acoustic thickness). To avoid noise in the simulation due to the discretization imposed by the grid required that the grid element size be less than the minimum acoustic wavelength generated. This is defined by the dimensions of the convoluted source and, ultimately, the laser-pulse duration. The upper limit was given by the laser-pulse time τ = 10 ns, requiring a grid element size smaller than $c\tau$ = 15 μm. A grid element size of 10 μm was therefore used.

The source was initially located at a distance of z = 3.5 mm directly above the detector. Figure 3(a) shows the effect of translating the source from this initial position by an amount Δy in the y direction. With increasing Δy, the signal shifts to the right owing to the increased source–detector distance, and its amplitude drops rapidly, falling by almost an order of magnitude for Δy = 1.5 mm. Figure 3(b) shows the effect of moving the source from the same initial position along the x direction. The corresponding decrease in signal amplitude for Δx = 1.5 mm is much smaller at a factor of 2. This indicates that the anisotropic response of a detector of these dimensions, and for this source geometry, will define a detection slice of approximately 2-mm thickness at z = 3.5 mm. To check that the directional characteristics of the source (owing to its finite size) were not influencing the simulated directivity in the length dimension of the detector, we repeated the simulation in Fig. 3(a) using a source diameter of 50 μm. All other parameters remained the same. The decrease in the signal amplitude with Δy was almost identical to that shown in Fig. 3(a), indicating that, for these detector dimensions, the upper limit of the detection slice thickness is defined largely by the detector geometry.

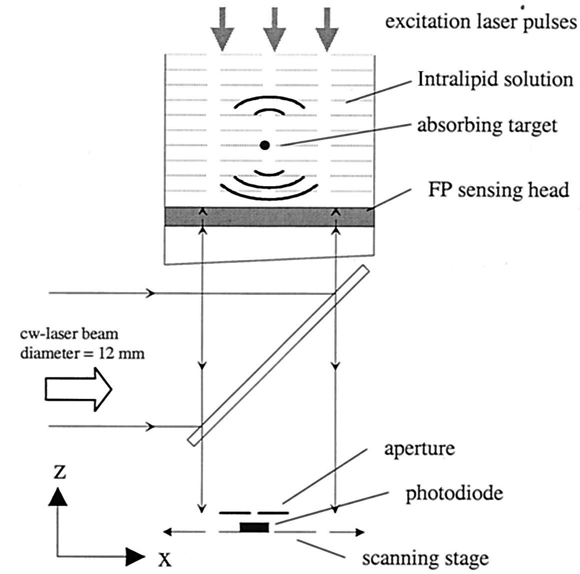

Fig. 4. Experimental imaging setup based on a line-scanned FP polymer-film sensing interferometer.

3. Experimental

In this section the reconstruction methods described in Subsection 2.A and the use of a rectangular detector geometry are evaluated experimentally. In all the images shown, no filtering of the measured signals or image enhancement was employed. A linear gray scale was used for all images.

A. Experimental Setup

Figure 4 shows a schematic of the experimental setup used. The excitation light source was a Q-switched Nd:YAG laser (λ = 1064 nm, pulse energy = 26 mJ, pulse duration = 6 ns, and repetition rate = 20 Hz).

The output of the laser was expanded to a diameter of 6 mm by use of a negative lens and used to irradiate the surface of a 10% aqueous solution of Intralipid-10% with a peak fluence of 0.2 J/cm^2. The approximate values of the optical coefficients of the solution were $\mu_a = 0.14$ cm^{-1} and $\mu_s' = 10$ cm^{-1}. These values were chosen to simulate the strong optical scattering of soft tissues. Absorbing targets, fabricated by laser printing of dots or lines onto acetate sheets, were immersed in the Intralipid. The photoacoustic signals generated by the irradiated absorbing regions were detected at the bottom of the Intralipid bath in the so-called forward or transmission mode. The ultrasound detector was a 75-μm-thick polyethylene terepthalate FP polymer-film sensing interferometer bonded to a 4-mm-thick impedance-matched polymethylmethacrylate backing stub.[14] The interferometer was illuminated by a collimated 60-mW, 850-nm diode-laser beam with a 12-mm $1/e^2$ diameter, and the reflected output beam was detected by use of a 25-MHz photodiode of diameter 0.8 mm mounted on a personal computer–controlled scanning stage.[15] An angle-tuned phase bias control system (not shown in Fig. 4) was used to set the working point of the interferometer to obtain the optimum sensitivity as described in Ref. 3. Photoacoustic signals arriving at the sensing film modulate its optical thickness and hence its reflectivity. By scanning the photodiode along a line across the reflected output beam and acquiring the detected waveform at each step of the scan, one can simulate a linear array of ultrasound detectors with this system. Signal averaging over less than 100 laser shots was used to obtain the experimental data described in Subsection 3.B. The signal-acquisition time was approximately 10 s/scan step.

The detectivity of the sensor was ~5 kPa (over a 25-MHz measurement bandwidth without signal averaging) and the frequency response was 15 MHz—a performance comparable with piezoelectric polyvinylidene fluoride transducers.[16] A key advantage over piezoelectric transducers is that the geometry of the detector element is defined by the area of the polymer sensing film that is optically addressed. Arbitrary acoustic detection geometries can therefore be achieved by placement of an appropriately shaped aperture in front of the photodiode. Thus a rectangular slit aperture was used to obtain the anisotropic response characteristics discussed in Subsection 2.B.

B. Evaluation of Two-Dimensional Reconstruction Algorithms

In the first instance, the objective was to evaluate the image-reconstruction process without introducing possible artifacts that are due to imperfect rejection of out-of-plane signals by a rectangular detector geometry. We therefore used a circular detector geometry that approximated to an isotropic detector and limited the source geometry to two dimensions by designing it to be constant in the y direction, $p_0(x, y, z) = p_0(x, z)$—assumption 2 in Subsection 2.A. The practical implementation of this was achieved by laser printing a series of strongly absorbing parallel lines of 180-μm width and 400-μm separation onto a transparent acetate sheet as shown in Fig. 5. This was immersed in the Intralipid solution and placed parallel to, and 3 mm above, the detection plane (x–y). When irradiated with pulsed laser light, the target approximates to a series of parallel line sources, each emitting cylindrical waves. When the detector (of 0.2-mm diameter) is scanned perpendicularly to the lines, only the photoacoustic signals emitted by that part of each line source that intersects the detection plane (the x–z plane containing the scan line) arrive at the detector.

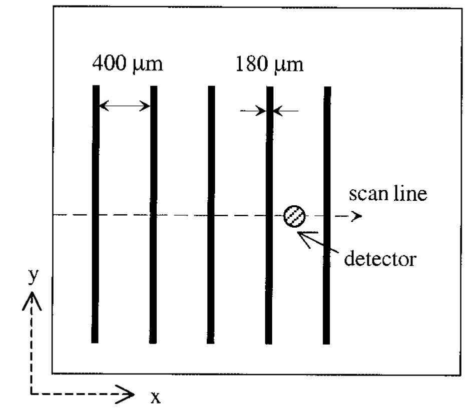

Fig. 5. Line-source target used to evaluate image-reconstruction algorithms. The detector diameter was 0.2 mm.

Figure 6(a) shows the photoacoustic waveforms $p(x, t)$ detected at 100-μm steps over a 10-mm line scan. The image clearly shows the cylindrical nature of the waves emitted from each line source with the envelope of the initial wave fronts at approximately 2 μs, corresponding to the 3-mm source–detector distance. Figure 6(b) shows the image reconstructed from the detected photoacoustic signals by use of the Fourier-transform algorithm described in Subsection 2.A. For comparative purposes, a reconstruction that uses the radial backprojection method described in Subsection 2.A is shown in Fig. 6(c). The same number of image pixels (208 $\times$ 482) were used in both cases.

The images reconstructed by both methods accurately show the general features of the target, for example, the correct height and separation of the sources. However, because the backprojection reconstruction in Fig. 6(c) involves distributing the signal amplitude over an arc, and therefore into regions of the image that should be of zero intensity, there are inevitably artifacts: Circular arcs can be clearly seen around each of the reconstructed line absorbers. In contrast, fewer artifacts are seen in the Fourier-transform reconstructed image because it approximates (subject to the limited dimensions of the line scan and spatial and temporal discretizations in the detection process, etc.) an exact solution. A further important advantage is that the Fourier-based algorithm is computationally much more efficient: It takes 11 μs/reconstructed image pixel, whereas the

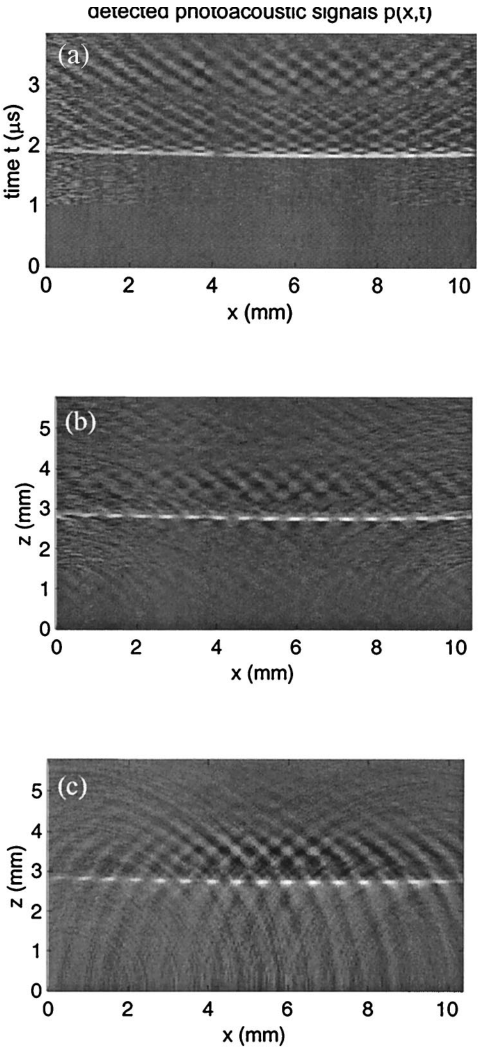

Fig. 6. Evaluation of image-reconstruction algorithms by use of the source–detector geometry depicted in Fig. 5. (a) Photoacoustic signals $p(x, t)$ detected at each point of the line scan by use of a circular detector of diameter 0.2 mm, (b) the image reconstructed from $p(x, t)$ by use of the Fourier-transform algorithm, and (c) the image reconstructed by use of the radial backprojection method.

backprojection algorithm takes approximately 3 ms/pixel by use of a MATLAB code on a 1-GHz personal computer. The total reconstruction time for the images in Figs. 6(b) and 6(c) (both of which contain 208×482 pixels) was approximately 1 s and approximately 5 min, respectively.

The expanded view of Fig. 6(b) in Fig. 7 shows two of the reconstructed absorbing lines. The width of these is approximately 200 μm and is in good agreement with the known width of 180 μm. The lateral resolution is, by analysis of the edges of the reconstructed features, conservatively estimated at 200 μm. The thickness of the ink deposited onto the acetate sheet is not known accurately but is likely to be significantly less than 10 μm, thus approximating a spatial impulse function in the vertical direction. Thus, by measuring the thickness of one of the reconstructed features in Fig. 7, we can estimate the vertical spatial resolution at 60 μm, limited by the 75-μm thickness of the detector.

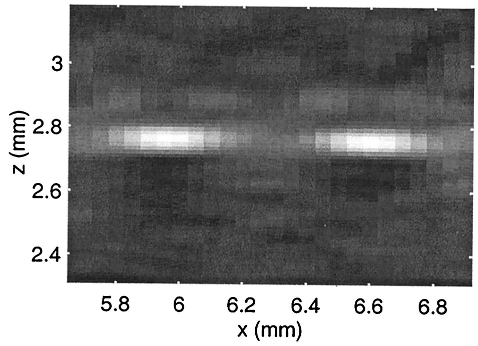

Fig. 7. Expanded view of Fig. 6(b) [Fourier reconstructed image $p_0(x, z)$].

To assess the effect of possible uncertainty in the source distribution in the y direction, as discussed in Subsection 2.B, we repeated the radial backprojection reconstruction using cylindrical ($1/\sqrt{r}$) and spherical spreading attenuation functions ($1/r$). Apart from a near uniform scaling factor, there was no discernable difference between these images and Fig. 6(c).

C. Two-Dimensional Imaging That Uses a Rectangular Detector Element Geometry

In Subsection 3.C.1 the basic principle of rejecting out-of-plane signals by use of a rectangular detector is demonstrated, and in Subsection 3.C.2 the geometrical parameters of the reconstructed image slice are determined.

1. Comparison of Circular and Rectangular Detector Geometries

To evaluate the use of a rectangular detector for 2D imaging, we used a well-defined geometrical arrangement of near-omnidirectional sources distributed inside and outside the detection slice (Fig. 2 shows a 3D representation of the geometry). This consisted of a horizontal line of absorbing dots of diameter 200 μm and separated by 800 μm printed onto an acetate sheet (Fig. 8) and submerged in the scattering solution. The target was situated at a distance $z = 3.2$

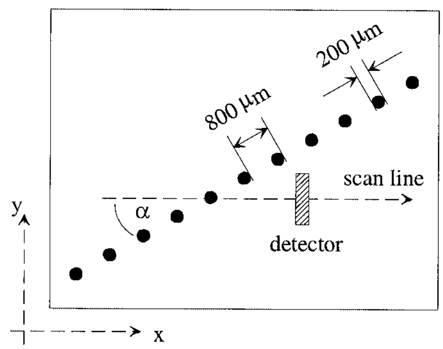

Fig. 8. Point-source target used to assess degree of out-of-plane signal rejection by use of a rectangular (800 μm × 200 μm) detector. $\alpha = 30°$.

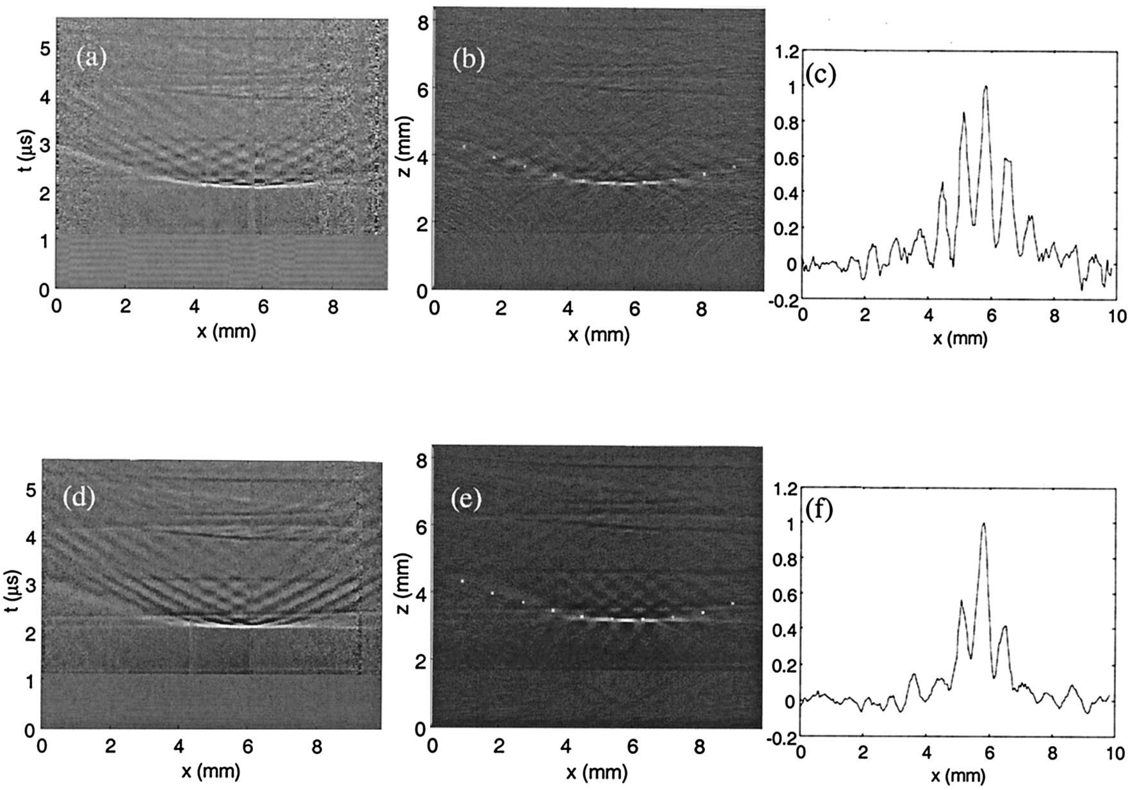

Fig. 9. Influence of detector geometry. (a) Photoacoustic signals $p(x, t)$ detected at each point of a line scan of the point-source target (Fig. 8) by use of a circular detector of diameter 0.2 mm, (b) the image reconstructed from these signals, and (c) the profile along the curve of x symbols superposed on (b). The corresponding detected photoacoustic signals, reconstructed image, and profile for a rectangular detector of dimensions 800 μm × 200 μm are shown in (d), (e), and (f), respectively.

mm above the detection line. The detector was scanned along a 10-mm line in 50-μm steps at an angle of $\alpha = 30$ deg to the line of absorbing dots. Only those dots that lie in the geometrical line of sight vertically above the detector are in-plane sources; the remaining dots are out of plane. This arrangement provides a convenient means of assessing the degree of rejection of the out-of-plane signals and, ultimately therefore, the thickness of the reconstructed image slice.

Two line scans of the target shown in Fig. 8 were carried out. In the first scan, a 200-μm circular aperture was placed in front of the photodiode to create a detector that approximates to one with an isotropic response. The purpose of this scan was to check that the absorbing dots emit acoustic energy into a sufficiently large solid angle such that signals from the out-of-plane sources actually arrive at the detector line scan. In the second scan, a rectangular slit aperture of dimensions 800 μm × 200 μm was placed in front of the photodiode. The photoacoustic signals detected over both line scans, and the corresponding reconstructed images are shown for both detector geometries in Fig. 9.

Figure 9(a) shows the signals detected by use of the circular aperture, and Fig. 9(d) shows those detected by use of the rectangular aperture. The most noticeable difference between the two is the nature of the envelope of the initial wave fronts. With the 200-μm circular aperture, it is curved because the detector approximates an isotropic receiver of low directional sensitivity and therefore detects signals from each of the absorbing dots. The signals from the dots at the beginning and end of the scan arrive at later times while the signals from the dots at the center of the scan, where the detector passes directly beneath them, arrive at earlier times. In contrast, the envelope of the initial wave fronts obtained with the rectangular detector in Fig. 9(d) is flat—its lateral extent is also less than in Fig. 9(a). The dots, which produce the signals that lie on this envelope, must therefore all be situated the same distance from the detector, and, because the temporal position of the envelope (~2.1 μs) is the same as the minimum of the curved wave-front envelope in Fig. 9(a), these dots must lie vertically above the detector. This shows that only the signals from the in-plane sources (see Fig. 2) at the center of the scan are detected; the remaining out-of-plane signals are not registered.

These observations are confirmed by the reconstructed images in Figs. 9(b) and 9(e). In the image in Fig. 9(b), obtained by use of the 200-μm circular aperture, the reconstructed dots are distributed at different heights z' along a curve because of the varying source–detector distance along the scan line. The equation of this curve is given by

$$z'^2 = z^2 + \Delta y^2,$$

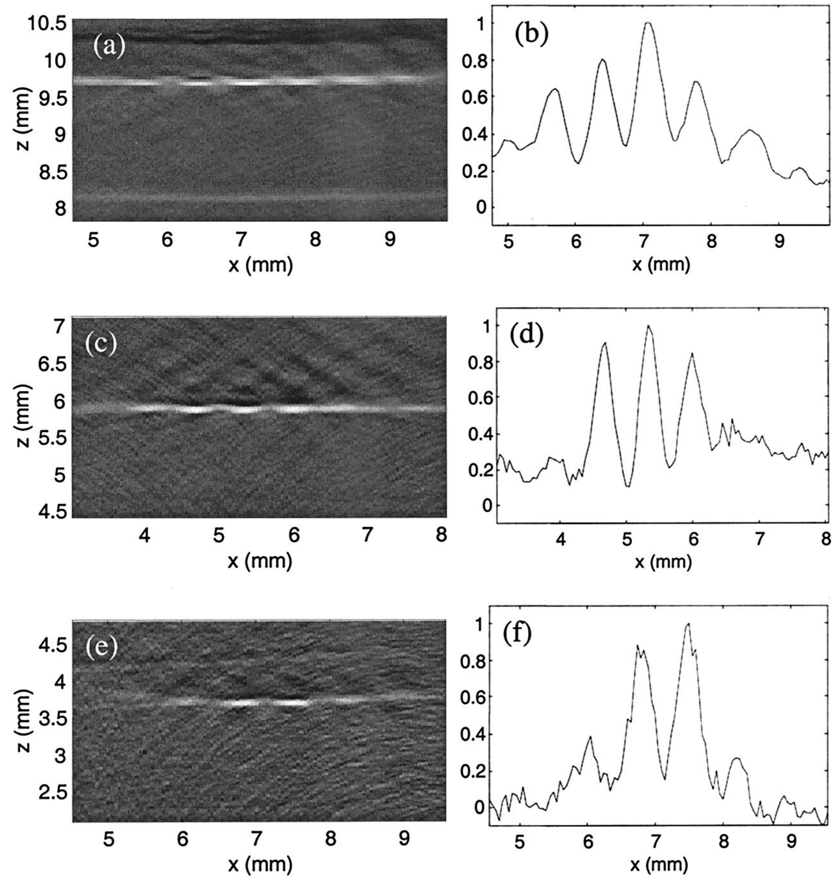

Fig. 10. Image slice thickness as a function of z. Reconstructed images of point-source target (Fig. 8) situated at three depths (reconstructed image): (a) $z = 3.7$ mm, (c) $z = 5.84$, and (e) $z = 9.66$ mm. (b), (d), and (f) show the horizontal profiles through the reconstructed dots for each image, illustrating the increasing image slice thickness with z of 9.66, 5.84, and 3.7, respectively.

where

$$\Delta y = \Delta x \tan \alpha, \tag{9}$$

and Δy is the distance in the y direction from a particular dot to the scan line (Fig. 8). Δx is the distance in the x direction from the dot to the point at which the scan line intersects with the line of dots. z' therefore is the distance from the line of dots to the detection line as a function of x and manifests itself as the x-dependent vertical height z' of the sources in the reconstructed images. A curve of small x symbols according to Eq. (9) is superposed on the image in Fig. 9(b) and is in good agreement with the position of the reconstructed sources. The amplitude profile along this curve is shown in Fig. 9(c). Note that if both source output and detector sensitivity were truly omnidirectional all the reconstructed dots would [assuming the influence of $a(r)$ is negligible] be of near-equal intensity. As neither of these conditions are wholly fulfilled, the intensity of the dots significantly diminish the farther they are from the scan line.

In Fig. 9(e), which was obtained by use of the rectangular detector, the reconstructed dots lie along a straight horizontal line as only the signals emitted by sources lying in the detection slice are detected, and all these sources are the same distance from the detector. As a consequence, Eq. (9) does not fit, and therefore fewer dots appear in the profile in Fig. 9(f). These results demonstrate the basic principle of defining an image slice by use of a rectangular detector element geometry. In Subsection 3.C.2 the thickness of the image slice and the typical spatial resolution are determined.

2. z-*Dependent Image Slice Thickness*

To measure the thickness ΔY of the reconstructed slice as a function of z, we placed the target shown in Fig. 8 at three different vertical distances above the detection plane ($z = 3.7$ mm, $z = 5.84$ mm, $z = 9.66$ mm) and scanned the target with the rectangular detector as described in Subsection 3.C.1. The reconstructed images and corresponding horizontal straight-line profiles are shown in Fig. 10. With increasing z, more of the dots are located within the divergent far-field zone of the detector. The reconstructed image slice thickness ΔY therefore increases as evidenced by the images in Figs. 10(a), 10(c), and 10(e), which show more reconstructed dots as z is increased. One can obtain ΔY by estimating the number n of visible dots in the images, multiplying by the known dot separation of $s = 800$ μm, and projecting onto the y axis. Thus

$$\Delta Y = (n - 1)s \sin \alpha. \tag{10}$$

For $z = 3.7$ mm, Fig. 10(e) indicates that $n \sim 3$. ΔY is therefore approximately 0.8 mm. In that this is the length dimension of the detector, this depth corresponds to the near-field receive zone. For greater source–detector distances, the receive zone begins to diverge as evidenced by the increasing number of visible dots in Fig. 10 with increasing z. By use of Eq. (10) for $n = 4$ at $z = 5.84$ mm in Fig. 10(c), $\Delta Y = 1.2$ mm, and, for $n = 6$ at $z = 9.7$ mm in Fig. 10(a), $\Delta Y = 2$ mm. The lateral resolution, which also increases with z, is estimated to be in the range 200–250 μm for the images in Fig. 10. The vertical resolution (as in Subsection 3.B) is estimated at 60 μm for all three images in Fig. 10. It is limited by the detector thickness and largely independent of z.

4. Conclusion

Aspects of 2D biomedical photoacoustic imaging have been explored. The Fourier-transform-based reconstruction algorithm has been demonstrated to provide a more accurate and faster reconstruction than simple backprojection methods. With a reconstruction time of 1 s for a 10^5 pixel image, it is suitable for applications in which patient movement or the need to monitor dynamic physiological events demands near-real-time image reconstruction.

The use of a rectangular detector geometry to reject out-of-plane signals for the practical implementation of 2D imaging has been demonstrated by use of a line-scanned FP ultrasound sensor. A key parameter is the reconstructed image slice thickness. For structures of the order of several hundred micrometers located as far as 1 cm from the detector, an image slice thickness varying from 0.8 mm at $z = 0$ to 2 mm at $z = 10$ mm was obtained by use of a rectangular detector of length dimension $L = 800$ μm. This would be suitable for short-range applications such as imaging superficial blood vessels. For longer-range applications such as imaging breast tumors to depths of several centimeters, the slice thickness aspect ratio would be optimized by making L significantly larger ($\sim$1 cm) to extend the nondivergent near-field receive zone.

The FP polymer-film sensing concept has been shown to be an ideal detection system for evaluating the concepts explored in this paper. In particular, the ability to define arbitrary detection geometries is an important advantage over discrete piezoelectric transducers. Although strongly absorbing targets that resulted in relatively high-amplitude signals were used in this investigation, this type of sensor has previously been shown to have sufficient sensitivity to detect the weaker photoacoustic signals generated in more realistic tissue phantoms. For example, absorbers with optical properties similar to blood, submerged in Intralipid ($\mu_a = 0.03\ \mathrm{mm}^{-1}$ and $\mu_s' = 1\ \mathrm{mm}^{-1}$) have been imaged to a depth of 2 cm with this concept.[3] To advance to practical biomedical imaging, it now remains to configure the sensor head for backward-mode use and implement a multielement photodiode array to reduce data-acquisition time.

K. Köstli is supported by an IHP fellowship of the Swiss Science Foundation SNF (83EU-065585). P. Beard is supported by an Engineering and Physical Sciences Research Council Advanced Fellowship.

References and Note

1. C. G. Hoelen, F. F. de Mul, R. Pongers, and A. Dekker, "Three-dimensional photoacoustic imaging of blood vessels in tissue," Opt. Lett. **23,** 648–650 (1998).
2. R. G. Kolkman, M. C. Pilatou, W. Steenbergen, and F. F. de Mul, "Photoacoustic monitoring and imaging of blood vessels in tissue," in *Biomedical Optoacoustics III*, A. A. Oraevsky, ed., Proc. SPIE **4618,** 76–80 (2002).
3. P. C. Beard, "Photoacoustic imaging of blood vessel equivalent phantoms," in *Biomedical Optoacoustics III*, A. A. Oraevsky, ed., Proc. SPIE **4618,** 54–62 (2002).
4. A. A. Oraevsky, E. V. Savateeva, S. V. Solomatin, A. Karabutov, V. G. Andreev, Z. Gatalica, T. Khamapirad, and P. M. Henrichs, "Optoacoustic imaging of blood for visualization and diagnostics of breast cancer," in *Biomedical Optoacoustics III*, A. A. Oraevsky, ed., Proc. SPIE **4618,** 81–94 (2002).
5. J. A. Viator, G. Au, G. Paltauf, S. L. Jacques, S. A. Prahl, H. Ren, Z. Chen, and J. S. Nelson, "Clinical testing of a photoacoustic probe for port wine stain depth determination," Lasers Surg. Med. **30,** 141–148 (2002).
6. R. A. Kruger, K. K. Kopecky, A. M. Aisen, D. R. Reinecke, G. A. Kruger, and W. L. Kiser, "Thermoacoustic CT with radio waves: a medical imaging paradigm," Radiology **211,** 275–278 (1999).
7. K. P. Köstli, M. Frenz, H. P. Weber, G. Paltauf, and H. Schmidt-Kloiber, "Optoacoustic tomography: time-gated measurement of pressure distributions and image reconstruction," Appl. Opt. **40,** 3800–3809 (2001).
8. O. T. Von Ramm and S. W. Smith, "Beam steering with linear arrays," IEEE Trans. Biomed. Eng. **BME-30,** 439–451 (1983).
9. G. J. Diebold and T. Sun, "Properties of photoacoustic waves in one, two and three dimensions," Acustica **80,** 339–351 (1994).
10. The Grüneisen coefficient is given by $\Gamma = B\beta/\rho C$, where B is the bulk modulus, β is the coefficient of volume thermal expansion, ρ is the density, and C the isobaric specific heat.
11. L. D. Landau and E. M. Lifshitz, *Fluid Mechanics*, 2nd ed. (Butterworth-Heinemann, Oxford, UK, 1987).
12. K. P. Köstli, M. Frenz, H. Bebie, and H. P. Weber, "Temporal backward projection of optoacoustic pressure transients using Fourier transform methods," Phys. Med. Biol. **46,** 1863–1872 (2001).
13. K. P. Koestli, D. Frauchiger, J. J. Niederhauser, G. Paltauf, H. P. Weber, and M. Frenz, "Optoacoustic imaging using a three-dimensional reconstruction algorithm," IEEE J. Sel. Top. Quantum Electron. **7,** 918–923 (2001).
14. P. C. Beard, F. Perennes, and T. N. Mills, "Transduction mechanisms of the Fabry Perot polymer film sensing concept for wideband ultrasound detection," IEEE Trans. Ultrason. Ferroelectr. Freq. Control **46,** 1575–1582 (1999).
15. P. C. Beard and T. N. Mills, "2D line scan photoacoustic imaging of absorbers in a scattering tissue phantom," in *Biomedical Optoacoustics II*, A. A. Oraevsky, ed., Proc. SPIE **4256,** 34–42 (2001).
16. P. C. Beard, A. Hurrell, and T. N. Mills, "Characterization of a polymer film optical fiber hydrophone for the measurement of ultrasound fields for use in the range 1–30 MHz: a comparison with PVDF needle and membrane hydrophones," IEEE Trans. Ultrason. Ferroelectr. Freq. Control **47,** 256–264 (2000).